Novel epoxy powder for manufacturing thick-section composite parts under vacuum-bag-only conditions. Part I: Through-thickness process modelling

Novel epoxy powder for manufacturing thick-section composite parts under vacuum-bag-only conditions. Part I: Through-thickness process modelling

James. M. Maguire [a,*], Pavel Simacek [b], Suresh G. Advani [b] Conchúr M. Ó Brádaigh [a]

[a] *School of Engineering, Institute for Materials and Processes, The University of Edinburgh, Edinburgh, EH9 3FB, UK*

[b] *Department of Mechanical Engineering and Center for Composite Materials, University of Delaware, Newark, DE 19716, USA*

** Corresponding author. Email address: j.maguire@ed.ac.uk*

Abstract

Thick-section composite parts are difficult to manufacture using thermosetting resins due to their exothermic curing reaction. If processing is not carefully controlled, the build-up of heat can lead to warpage or material degradation. This risk can be reduced or removed with the use of a low-exotherm resin system. Material and process models are presented which describe vacuum-bag-only processing of thick-section composites using a novel, low-exotherm epoxy powder. One-dimensional resin flow and heat transfer models are presented which govern the fabric impregnation and temperature evolution, respectively. A semi-empirical equation is presented which describes the sintering of the epoxy powder. The models are coupled via laminate thickness change, which is determined for a simplified ply microstructure. The resulting system of equations are discretised and solved numerically using a finite difference code. A case study is performed on a 100-ply laminate, and the advantages and disadvantages of using epoxy powders are discussed.

Keywords: A. Epoxy powder, C. Process modelling, E. Consolidation, E. Cure

1. Introduction

The concept of using polymer powders for composite manufacturing has been explored since the 1970s [1]. In the late 1980s and early 1990s, NASA and supporting academics conducted several investigations into ‘towpregging’ and tape production using both thermoplastic and thermosetting powders [2–5]. More recently, significant research has been focused on the use of epoxy powders for the production of low-cost, vacuum-bag-only (VBO) prepregs, which

can be used to manufacture wind and tidal turbine blades (e.g. European projects MARINCOMP and POWDERBLADE). These projects investigated the processing of epoxy powder composites [6–8] and their mechanical performance [9–11]. The results of the projects showed that epoxy powder composites were mechanically comparable to conventional epoxy composites used by the wind energy industry. They also revealed that the epoxy powder has several processing advantages which make it well suited to the VBO prepreg format. Firstly, the epoxy powder could maintain a viscosity of 10 – 100 Pa s for up to 3 hr at 120°C, which is low enough to infuse glass-fibre (GF) and carbon-fibre (CF) fabrics when using a VBO prepreg format [8]. Secondly, the epoxy powder has excellent storage stability which means that the epoxy powder doesn't suffer from 'out-time' curing effects to the same extent as conventional epoxy-based VBO prepregs (i.e. they could be left at ambient conditions for several months without any significant change in the degree of cure (DoC)). Its chemical stability at temperatures up to 120°C also provides the potential to infuse composite parts separately (e.g. wind turbine blade skins, spars, shear webs, etc.), and then co-cure them to form a "one-shot" structure without the need for adhesive bonding [6]. In terms of its curing behaviour above 120°C, the epoxy powder produces relatively little exothermic heat (< 200 J/g) compared to conventional epoxies (e.g. 400 – 600 J/g), which is significant for the manufacture of thick-section components due to the risk of "thermal runaway" [8].

While the aforementioned results showed the potential of the epoxy powder, the material characterisation experiments focussed on processing small samples using programmed temperature cycles. In practical terms, however, manufacturing thick-section composite parts is significantly more complex. It has been shown that the initial state of the powder-based composite can affect how the material is processed; Ramasamy et al. [12] noted that braiding with powder-coated towpregs was challenging due to the increased bulk of the tows and preform. Moreover, for thick-sections, temperature divergence from the programmed temperature cycle is unavoidable due to the lag in heat transfer, particularly in the centre of the laminate [13]. It is impossible to know whether the overall manufacturing process will benefit from the seemingly advantageous characteristics of the epoxy powder without taking a more holistic view of the system. This system includes key processes such as resin flow and heat transfer, which can be modelled mathematically.

The modelling and simulation of flow processes in composite materials has undergone a great deal of development in the last three decades, owing largely to the advent of liquid composite moulding (LCM) processes [14]. In most cases, thermoset resin flow through a fibre-bed has

been modelled using Darcy's Law as the governing equation [15]. Numerous resin flow models have been developed to describe manufacturing methods which utilise through-thickness flow (e.g. Resin Film Infusion (RFI), Compression Resin Transfer Moulding (CRTM), VBO prepregs, etc.) [16–18]. These models vary in their complexity depending on the processing phenomena which they describe. For VBO prepregs (a.k.a. out-of-autoclave (OoA) prepregs), plies are partially impregnated by resin, which means the resin is only required to flow into the adjacent plies. This a less complex flow problem than RFI or CRTM where resin must flow through an entire preform. As such, some resin flow models for VBO prepregs have been comparatively simple. Centea and Hubert [18] used Darcy's Law to model the process as one-dimensional (1D) radial resin flow into the fibre tows, using an equivalent hydraulic radius R_t for the elliptical geometry of the tows. Alternatively, the resin flow in VBO prepregs can be considered dual-scale in nature [19]; macroscopic flow around the fibre tows (inter-tow flow), and microscopic flow within the fibre tows (intra-tow flow), with up to four orders of magnitude difference between the permeabilities of these regimes [20,21]. Cender et al. [19] modelled the dual-scale flow phenomena as 1D resin flow through two porous media in series; assuming that the resin would fill the inter-tow region entirely before beginning to impregnate the intra-tow region due to the difference in permeabilities.

It should be noted that these VBO prepreg resin flow models were used to simulate the processing of thin laminates only (< 4 mm thick), with simplified assumptions made for the temperature conditions. For example, Cender et al. [19] assumed isothermal conditions for their experiments and were able to solve the resin flow problem analytically, while Centea and Hubert [18] input the time-temperature data directly into the model and assumed uniform temperature throughout the laminate. For thick-section composites, a uniform temperature distribution cannot be assumed because large temperature gradients are known to develop within the laminates due to the inherent insulating properties of the fibres and polymer matrix. This is compounded by using exothermic thermosetting resin systems which can cause "thermal runaway" of the composite part during manufacture, as previously mentioned. As a result, a considerable amount of research has been carried out on heat transfer modelling of thick-section composite parts manufactured using thermosetting prepregs. Several heat transfer models for thick-section composites were developed in the 1980s and early 1990s [13,22–25]. For these models, heat transfer within the laminate was described using the well-known heat equation with an additional term for heat generation from the exothermic curing reaction.

In general, the aforementioned publications vary in terms of whether or not they account for consolidation of the thick-section laminate. Bogetti and Gillespie [13] opted not to model consolidation, due to the added complexity of modelling in 2D, however, they acknowledged that thickness effects would strongly influence the processing of thick sections. With simulations, they demonstrated that increasing laminate thickness created a thermal lag between the prescribed temperature cycle and the centre of the laminate. Building on this, Twardowski et al. [25] implemented approximations for consolidation (based on either uniform linear or exponential change in FVF over a set period of time) and found that it had a significant effect on heat transfer in the laminate during processing. This trend was corroborated by Shi [26] via analytical models, numerical simulations, and experiments. Oh and Lee [27] modelled both heat transfer and consolidation, however, the simulations were performed separately so that the models were not fully coupled i.e. data from the heat transfer model was input into the consolidation model, but not vice versa. Shin and Hahn [28], on the other hand, developed a finite difference code which fully coupled resin flow and heat transfer of a thick prepreg laminate processed in a heated press.

Initial work on the process modelling of thick-section epoxy powder-based composites began with a focus using on coupling resin flow to heat transfer via cure kinetics and chemorheology, and coupling heat transfer to resin flow via thickness change [29,30], however, these models did not account for the thickness change due to powder sintering. The bulk volume of epoxy powder is up to twice the volume of fully sintered powder depending on the packing of particles. Greco and Maffezzoli [31] presented models to describe the melting and sintering of polymer powder. While polymer melting and sintering are linked, densification of the powder due to sintering does not occur instantaneously upon the polymer reaching its melting point. Instead, it is dependent on the viscosity and surface energy of the polymer [32]. Kandis and Bergman [33] developed an Arrhenius-type semi-empirical relation to describe the kinetics of the sintering process. Greco and Maffezzoli [31] fit this sintering model to thickness measurements from thermal mechanical analysis (TMA) and showed that it better described the densification of the powder than their original melting model.

Part I of this study focuses on the development of numerical models for simulating the manufacture of thick-section structures using epoxy powder technology. Process models are presented for coupled resin flow and heat transfer, and a semi-empirical model is introduced which describes the sintering of the powder. These models are combined with existing material models for the epoxy powder [8] to describe how temperature, viscosity, DoC, degree of

impregnation (DoI), and laminate thickness evolve during the manufacturing process. Experimental validation of the model and additional simulations are the subject of Part II of this study [34].

2. Methodology

2.1 Semi-empirical sintering model for epoxy powder

An epoxy powder system (GRN 918), supplied by ÉireComposites Teo., is considered in this study [35]. This system was previously characterised using thermogravimetric analysis (TGA), differential scanning calorimetry (DSC) and parallel-plate rheometry (PPR), and semi-empirical models were developed to describe its cure kinetics and chemorheological behaviour with respect to temperature [8].

For this study, a HAAKE MARS II rheometer (Thermo Scientific) was used to perform an additional set of PPR tests which measured the compaction of the powder due to sintering. Khoun et al. [36,37] showed that it was possible to measure the thickness change of an epoxy sample by monitoring the gap height between the parallel plates for a given normal force. For the MARS II rheometer, a Peltier module was used to heat the lower plate, and a PEEK sample hood was used for insulation. For all tests, the top plate was lowered onto the powder sample until it resisted compaction (the rheometer had a limiting normal force of 50 N). A normal force of 50 N was approximately equivalent to 52 kPa of pressure for the 35 mm plates that were used. Isothermal tests at 50°C, 55°C, and 60°C were carried out because these temperatures were near the glass transition temperature (T_g) of the epoxy powder; the temperature at which the powder would begin to sinter. The rheometer began recording the sample thickness as soon as the test temperature was reached. No resin squeeze-out was observed during testing due to the resin's high viscosity at the test temperatures (> 20,000 Pa s [8])

The results of the tests were fitted to a semi-empirical model developed specifically for GRN 918. Kandis and Bergman [33] previously modelled the polymer powder sintering process using an Arrhenius-type expression due to the exponential temperature dependence of the polymer viscosity [32] (i.e. as the viscosity reduces, the powder collapses due to surface energy or some external driving force). From chemorheological modelling of GRN 918, it was known that its viscosity reduction was best modelled using the Williams-Landel-Ferry (WLF)

equation [8]. As such, the results of the PPR testing were fitted to the following WLF-type model,

$$\frac{d\chi}{dt} = -\chi_E \exp\left(\frac{C_{\chi 1}[T - T_\theta]}{C_{\chi 2} + T - T_\theta}\right)(\chi - \chi_\infty)^B \quad (1)$$

Where χ_E is a pre-exponential rate constant, χ_∞ is the powder void fraction at $t = \infty$, T is temperature [K] at time t [s], and T_θ is the onset temperature for melting [K]. $C_{\chi 1}$, $C_{\chi 2}$ [K], and B are fitting constants. The powder void fraction χ at time t is described by,

$$\chi = 1 - \frac{\rho_r}{\rho_P} \quad (2)$$

Where ρ_P is the bulk density of the polymer, and the density ρ_r is determined using,

$$\rho_r = \rho_0 \frac{L_0}{L} \quad (3)$$

Where ρ_0 is the initial density of the powder, L_0 is the initial thickness of the powder samples, and L is the thickness at time t, which was measured using PPR.

The sintering model parameters for GRN 918 are given in Table 1. From the PPR tests, the initial powder void fraction was estimated as being approximately 0.503. This was confirmed by manually compacting the powder in a 5 ml graduated cylinder and weighing it on a microbalance.

Table 1. Parameters for the sintering model.

Parameter [units]	Value
χ_E	3×10^{-5}
$C_{\chi 1}$	11.5
$C_{\chi 2}$ [K]	24.5
T_θ [K]	313.48
χ_∞	0.0
B	0.5

$$\frac{d\chi}{dt} = -\chi_E \exp\left(\frac{C_{\chi 1}[T - T_\theta]}{C_{\chi 2} + T - T_\theta}\right)(\chi - \chi_\infty)^B$$

2.2 Resin flow

Vacuum-bag-only (VBO) prepregs are plies of fabric reinforcement partially impregnated with resin on one or both sides. When manufacturing thick laminates, a prescribed number of plies are stacked on top of each other, as shown in Figure 1. At the beginning of the manufacturing process, the lay-up of plies is effectively a system of alternating resin and fabric layers. As heat and pressure are applied, the resin viscosity drops, and the resin is forced to flow into the fabric layer, leading to a change in laminate thickness.

Figure 2 illustrates the resin flow pattern which is expected for an epoxy powder based VBO prepreg, i.e. resin flow around the fibre tows (inter-tow flow), followed by resin flow into the fibre tows (intra-tow flow). Note that, while Figure 2 serves to illustrate the dual-scale flow phenomena in VBO prepregs, VBO prepregs are usually partially impregnated with resin; meaning some of the inter-tow and intra-tow regions may already be filled. While the model developed by Centea and Hubert [18] is perhaps more accurate in modelling the porous media as an ellipse, it assumes that the initial degree of impregnation (DoI) has been advanced to the point that the inter-tow region is completely filled. This is not always the case as a lower DoI can increase the air permeability of the VBO prepreg [38], leading to improved gas evacuation and low porosity [39]. For epoxy powder VBO prepregs, the powder is dispersed on only one side of the VBO prepreg, meaning that the "dry side" of the VBO prepreg is not completely filled with powder, hence there is inter-tow space which the epoxy must fill. Given the high initial viscosity of the epoxy powder (measured as approx. 20,000 Pa s at 70°C [8]), relatively slow viscous resin flow can be expected in the inter-tow region when processing thick-section structures, despite the its high permeability (circa 10^{-9} m^2). Moreover, ÉireComposites Teo.'s recommended drying temperature for the epoxy powder ranges from 40°C to 55°C; at 40°C, the epoxy is solid with a viscosity approaching infinity, while, at 55°C, the powder sinters and has a viscosity of 5×10^6 Pa s (predicted using the chemorheological model from [8] – see Equation A.1). As such, both inter-tow and intra-tow resin flow are considered herein.

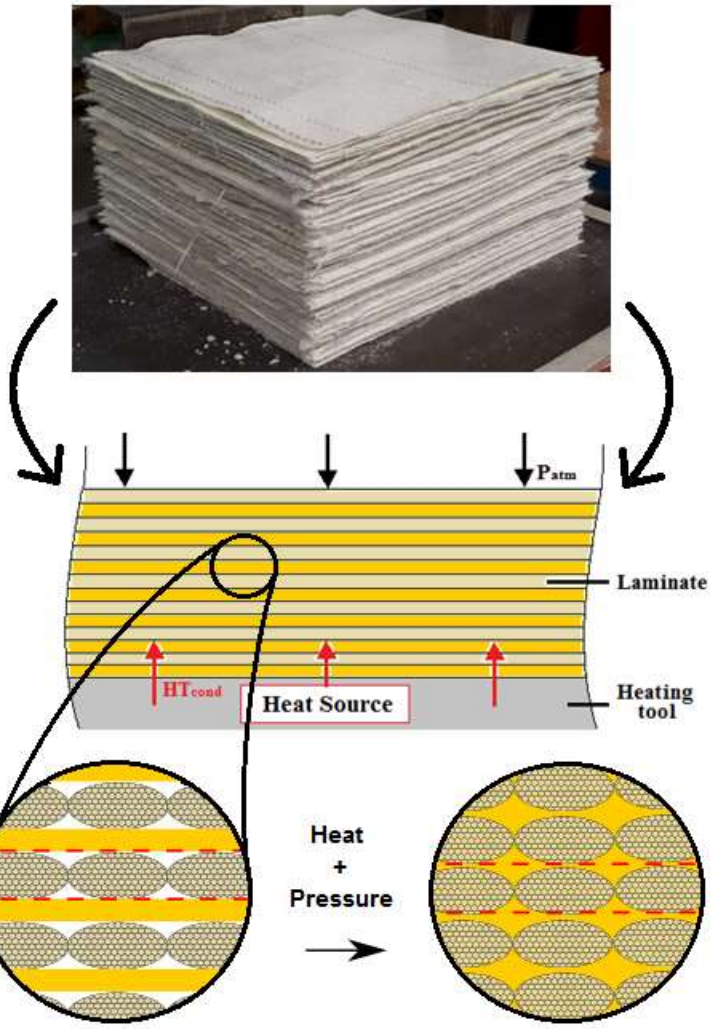

Figure 1. (Top) A thick laminate lay-up of glass-fibre/epoxy-powder VBO prepreg plies (60 plies). (Middle) Schematic representation of the VBO prepreg with alternating layers of resin and fabric. (Bottom) Zoomed-in images of the VBO prepreg arrangement. As heat and pressure are applied, the resin flows into the fabric layers.

For the model development, the following assumptions are made:

- Compaction due to gas evacuation is instantaneous
- The resulting fibre-bed is incompressible
- Nesting of fibre tows is negligible
- Resin flows through-thickness only (i.e. no in-plane flow)
- Resin flows into the adjacent fabric layers only (i.e. no global resin flow through multiple layers)

These assumptions simplify the governing equations for resin flow in VBO prepregs [18] compared to process models which consider the fibre bed compaction of VBO prepregs [40–42] or process models which consider resin flow through multiple layers of fabric [16,17].

Under these assumed conditions, there is a fixed volume of inter-tow space and intra-tow space that the resin could flow into and fill. The dual scale resin flow models developed by Cender et al. [19] are chosen as a suitable basis for modelling the epoxy powder VBO prepreg system. Some modifications are required, however, to adapt the equations for the highly transient temperature conditions of thick-section composite processing.

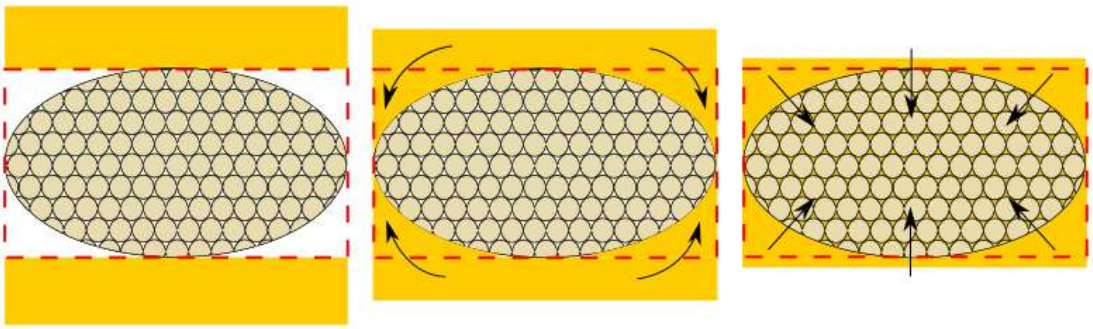

Figure 2. Schematic of the dual-scale flow pattern in VBO prepregs. (Left) If the DoI is zero, as shown no resin has flowed into the fabric layer (which is bounded by the red dashed line). (Middle) Resin flows first into the inter-tow space due to its higher permeability. (Right) Resin then flows into the low permeability tow.

To solve for transient temperature conditions (i.e. accounting for viscosity change due to temperature and DoC), Darcy's Law is written as,

$$\frac{dl}{dt} = -\frac{K}{\varphi\eta} \cdot \frac{dP}{dx} \tag{4}$$

Where l is the flow front position [m] at time t [s], K is the permeability [m^2], φ is the porosity, η is the resin viscosity [Pa s], which is temperature and cure dependent, and P is pressure [Pa].

Equation 4 is integrated over the pressure boundary conditions for inter-tow flow, $P|_{x=0} = P_{app}$ and $P|_{x=l} = 0$,

$$\int_0^l \frac{dl}{dt} dx = \int_{P_{app}}^0 -\frac{K}{\varphi\eta} \cdot \frac{dP}{dx} dx \quad , \quad l < L_1 \tag{5}$$

$$\frac{dl}{dt} = \frac{K_1}{\varphi_1\eta} \frac{P_{app}}{l} \quad , \quad l < L_1 \tag{6}$$

Where L_1 is the characteristic length of the inter-tow region [m], K_1 is the inter-tow permeability [m^2], φ_1 is the inter-tow porosity, and P_{app} is the pressure applied by the vacuum bag [Pa]. The viscosity along with the cure-dependent glass transition temperature (T_g) and the

DoC (α) are described using Equations A.1, A.2, and A.3, respectively, in Appendix A. Supplementary material.

For intra-tow flow, Equation 4 is integrated over pressure boundary conditions of $P|_{x=0} = P_{L1}$ and $P|_{x=l} = 0$,

$$\frac{dl}{dt} = \frac{K_2}{\varphi_2 \eta} \cdot \frac{K_1 P_{app}}{K_2 L_1 + K_1 (l - L_1)} \quad , \quad l \geq L_1 \tag{7}$$

Where the pressure at the boundary of the intra-tow region is,

$$P_{L1} = \frac{K_1 P_{app} (l - L_1)}{K_2 L_1 + K_1 (l - L_1)} \tag{8}$$

Where K_2 is the intra-tow permeability [m^2] and φ_2 is the intra-tow porosity. The derivation of Equation 8 is given in Appendix A. Supplementary material.

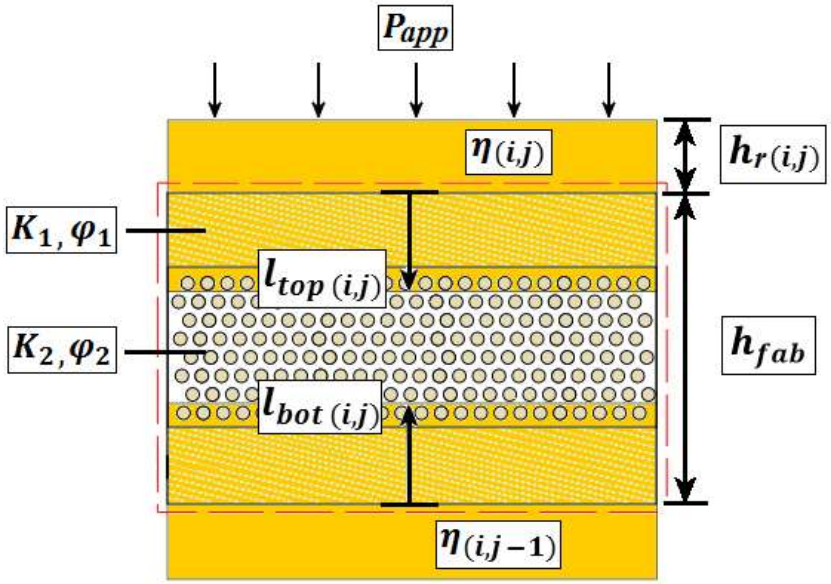

Figure 3. Physical representation of the 1D resin flow model at nodal position j and time step i. Resin flows into the fabric layer from above and below; in this case, the resin flow front position is defined as the distance from the inlet (dashed red line i.e. $x = 0$) to the flow front. The fabric layer is separated into inter-tow and intra-tow regions which are in series. The layer thicknesses are summed to calculate the total laminate thickness change.

Cender et al. [19] showed that the fill time is proportional to the square of the flow distance i.e. halving the flow distance results in a factor of four reduction in the time taken to fill the fabric. For this reason, it is important to account for resin flow into the fabric layer from above and

below, as illustrated in Figure 3. The total impregnation depth for each ply, $l_{tot(i,j)}$ [m] is found by combining the resin flow front position from the top ($l_{top(i,j)}$) and bottom ($l_{bot(i,j)}$),

$$l_{tot(i,j)} = l_{top(i,j)} + l_{bot(i,j)} \tag{9}$$

2.3 Thickness change

It is known that resin flow in VBO prepregs corresponds with a reduction in laminate thickness as the resin flows into the fabric layers [40,43]. For the finite difference code developed herein, a simplified ply microstructure is defined so that this thickness change can be computed. As mentioned in the previous section, it is assumed that compaction due to air evacuation has already occurred, and the fibre-bed is incompressible. The simplified ply microstructure is segmented into: a resin layer thickness, h_r [m]; a fabric layer thickness, h_{fab} [m]; and the total impregnation depth l_{tot} (see Figure 3). By summing these quantities, it is possible to determine the total laminate thickness, h_{lam} [m] for each time step i,

$$h_{lam,i} = \sum_{j=1}^{N_p} l_{tot(i,j)} + \sum_{j=1}^{N_p} (h_{fab} - l_{tot(i,j)}) + \sum_{j=1}^{N_p} h_{r(i,j)} \tag{10}$$

Where N_p is the number of plies in the laminate.

As impregnation progresses, the thickness of the resin layer diminishes from its initial value $h_{r(0,j)}$:

$$h_{r(i,j)} = h_{r(0,j)} - \beta\left(\varphi_{fab} h_{fab}\right) \tag{11}$$

Where φ_{fab} is the porosity of the fabric layer, and β is the degree of impregnation (DoI), which can be written as,

$$\beta = \frac{l_{tot}}{\varphi_{fab} h_{fab}} \quad , \quad l_{tot} < L_1 \tag{12}$$

$$\beta = \frac{\varphi_1 h_{fab} + (l_{tot} - \varphi_1 h_{fab})\varphi_2}{\varphi_{fab} h_{fab}} \quad , \quad l_{tot} \geq L_1 \tag{13}$$

The characteristic length, L_1 is assumed to be equivalent to the inter-tow thickness i.e. $\varphi_1 h_{fab}$.

Assuming that there are no significant gaps between tows in the same fabric layer (i.e. the vertices of each tow touch the vertices of the adjacent tows), the inter-tow porosity, φ_1 is

constant for an elliptical tow geometry, bound at its vertices and co-vertices by a rectangular cross-section (red dashed line in Figure 2),

$$\varphi_1 = \frac{A_{rec} - A_{ell}}{A_{rec}} = \text{constant} \cong 0.2146 \tag{14}$$

Where A_{rec} is the total area of the rectangular cross-section [m^2] outlined in Figure 2, and A_{ell} is the area of the elliptical tow [m^2].

For a known intra-tow porosity, φ_2, the porosity of the fabric layer, φ_{fab} is determined as follows [44,45],

$$\varphi_{fab} = \varphi_1 + \varphi_2 - \varphi_1\varphi_2 \tag{15}$$

For a fully impregnated ply, l_{tot} is equivalent to h_{fab} such that the second term on the righthand side of Equation 10 cancels. Naturally, the calculation of ply thickness, h_{ply} reduces to the sum of the fabric thickness and any excess resin layer that remains:

$$h_{ply} = h_{fab} + h_r \tag{16}$$

The resin volume fraction, φ, determines the quantity of resin in the ply and can be written as,

$$\varphi = \frac{\varphi_{fab}h_{fab} + h_r}{h_{fab} + h_r} \tag{17}$$

Rearranging,

$$h_r = h_{fab}\left(\frac{\varphi - \varphi_{fab}}{1 - \varphi}\right) \tag{18}$$

Note: in the case that φ is less than φ_{fab}, this term becomes negative and the code outputs an error messages warning that the plies will not achieve full impregnation.

Combining Equations 16 and 18, h_{fab} is approximated for a given φ,

$$h_{fab} = h_{ply}\left(\frac{1 - \varphi}{1 - \varphi_{fab}}\right) \tag{19}$$

As can be seen with the above set of equations, only the cured ply thickness (h_{ply}), the resin volume fraction (φ), and the intra-tow porosity (φ_2) are required to fully describe the ply microstructure shown in Figure 3. The cured ply thickness and the resin volume fraction can be measured experimentally, while values of intra-tow porosity can be found in the literature.

Another important consideration for modelling the thickness change is the initial form of the epoxy resin i.e. powdered or solid resin layer. For a powder layer, significant thickness reduction is expected during the sintering process. As such, the thickness of the resin layer, $h_{r(i,j)}$ is recalculated using,

$$h_{r(i,j)} = \frac{h^*_{r(i,j)}}{1 - \chi_{(i,j)}} \tag{20}$$

Where $h^*_{r(i,j)}$ is the thickness of the fully sintered resin layer, and the powder void fraction, $\chi_{(i,j)}$, is modelled using Equation 1.

2.4 Heat transfer

Transient one-dimensional (1D) heat conduction in a plane wall is used as the basis for the heat transfer model under the assumption that convective heat transfer due to resin flow is negligible [46,47]. The heat transfer equation is written using an explicit forward time, centred space finite difference formulation (illustrated in Figure 4). For the model developed here, Δz can vary as a function of resin flow in each fabric layer (i.e. heat transfer is coupled to the resin flow model via thickness change).

The structure of the heat transfer model is also approximated as individual layers of resin (h_r), fabric (h_{fab}), and impregnated fabric (l_{tot}) in series (see Figure 3). Each layer is treated as a separate material with a unique thermal conductivity, which can be modelled as thermal resistances in series. These resistances change based on the state of the resin (powder or liquid) and the progression of resin flow. The contact resistance between these layers is assumed to be negligible.

As such, the heat equation is approximated as,

$$\left(\frac{T_{i+1} - T_i}{\Delta t}\right)_j = \left(\frac{1}{\Delta z \rho c_P}\right)_{i,j} \left(\frac{T_{j-1} - T_j}{R_{j,j-1}} + \frac{T_{j+1} - T_j}{R_{j+1,j}}\right)_i + \left(\frac{m_r H_T}{c_P}\frac{d\alpha}{dt}\right)_{i,j} \tag{21}$$

Where subscripts i and j represent the time step and nodal position, respectively, T is temperature [K], Δt is the time step size [s], Δz is the element thickness of node j [m], ρ is density [kg/m^3], c_P is specific heat capacity [J/kg K], $R_{j,j-1}$ is the thermal resistance of the material [m^{2}K/W] between nodes j and $j-1$, m_r is the resin mass fraction, and H_T is the total enthalpy of the curing reaction [J/g], which is 184 J/g [8]. The final term in Equation 21 couples

heat transfer to the cure kinetics model, which is given by Equation A.3 in Appendix A. Supplementary material.

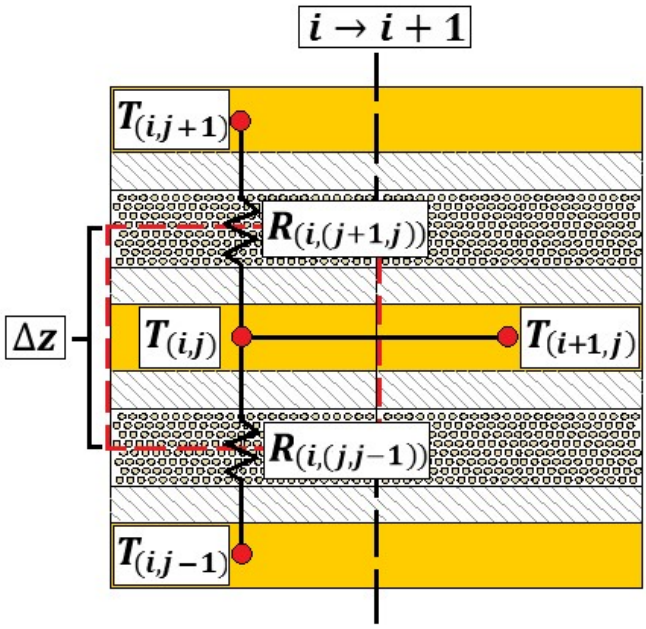

Figure 4. Illustration of the forward time, centred space scheme used for the heat transfer model. The temperature for the time step, $i+1$, is calculated explicitly based on the conditions at time step, i. The various layers of resin, dry fabric and impregnated fabric are approximated as thermal resistances in series.

The element thickness is approximated by,

$$\Delta z_{(i,j)} = h_{r(i,j)} + h_{fab} \tag{22}$$

The density of the material at each node is approximated by,

$$\rho_{(i,j)} = \rho_c \frac{h_{ply}}{h_{fab} + h_{r(i,j)}} \tag{23}$$

Where ρ_c is the composite density [kg/m^3], which is determined via the rule of mixtures. The specific heat capacity, c_P is also determined via the rule of mixtures method (see Appendix A. Supplementary material for the corresponding equations; Equations A.7 and A.8, respectively).

The thermal resistances $R_{(i,(j,j-1))}$ and $R_{(i,(j+1,j))}$ are written as,

$$R_{(i,(j,j-1))} = \frac{h_{r(i,j-1)}}{2\kappa_{r(i,j)}} + \frac{l_{tot(i,j)}}{\kappa_{c,T(i,j)}} + \frac{h_{fab} - l_{tot(i,j)}}{\kappa_{fab}} + \frac{h_{r(i,j)}}{2\kappa_{r(i,j)}} \tag{24}$$

$$R_{(i,(j+1,j))} = \frac{h_{r(i,j)}}{2\kappa_{r(i,j)}} + \frac{l_{tot(i,j+1)}}{\kappa_{c,T(i,j+1)}} + \frac{h_{fab} - l_{tot(i,j+1)}}{\kappa_{fab}} + \frac{h_{r(i,j+1)}}{2\kappa_{r(i,j+1)}} \quad (25)$$

Where κ_r is the thermal conductivity of the epoxy [W/m K], $\kappa_{c,T}$ is the transverse thermal conductivity of the impregnated composite [W/m K], and κ_{fab} is the thermal conductivity of the dry fabric [W/m K].

The resin mass fraction, m_r is:

$$m_{r(i,j)} = \frac{\rho_{r(i,j)}(1 - V_f)}{\rho_f V_f + \rho_{r(i,j)}(1 - V_f)} \quad (26)$$

Where V_f is the volume fraction.

2.5 Thermal boundary conditions

Two sets of boundary conditions (BCs) are considered for this work: specified temperature BCs for heated tooling; and forced convection BCs for oven heating. Heat transfer due to radiation is not modelled explicitly.

As described by Bogetti and Gillespie [13], the specified temperature BC is implemented by setting the surface node temperature at time step $i, T_{(i,s)}$ [K] equal to the programmed temperature cycle, $T_{P(i)}$ [K]:

$$T_{(i,s)} = T_{P(i)} \quad (27)$$

For describing heat transfer by forced convection, the following expression from Çengel [48] is used,

$$\rho c_P \frac{\Delta z}{2} \frac{T_{(i+1,s)} - T_{(i,s)}}{\Delta t} = h\left(T_{P(i)} - T_{(i,s)}\right) + \kappa \frac{T_{(i,s\pm1)} - T_{(i,s)}}{\Delta z} \quad (28)$$

Where h is the heat transfer coefficient (HTC) [W/m^{2}K], and $T_{(i,s\pm1)}$ is equal to $T_{(i,s+1)}$ for the bottom BC and $T_{(i,s-1)}$ for the top BC.

For forced convection BCs, Zimmermann and Van Den Broucke [49] recommended that a convective HTC of 10 – 100 W/m^{2}K be used for gases in an autoclave. Similarly, average convective HTCs have been experimentally measured in the range of 10 – 40 W/m^{2}K for autoclaves [50,51]. A convective HTC of 40 W/m^{2}K was chosen for all simulations in this study. The remaining material parameters in Equation 28 depend on the surface composition.

For VBO prepreg manufacturing it is expected that the top boundary would consist of bagging materials, while the bottom boundary would be the B-side of the mould tool. Oh and Lee [27] assumed negligible thermal contact resistance between the bagging, laminate, and tooling; the same assumption is made in this work. Conduction through any additional layers (i.e. tooling, bagging, insulation, etc.) is modelled for all BCs. These additional layers are also modelled as thermal resistances in series. The corresponding equations are given in Appendix A. Supplementary material.

2.6 Material properties

This work focusses on manufacturing simulations for GRN 918 epoxy powder with glass-fibre fabrics. Some important material characteristics of GRN 918 epoxy powder have already been discussed, however, additional data for thermal conductivity and specific heat capacity is required for heat transfer modelling. It is assumed that the specific heat capacity of GRN 918, as a function of temperature and DoC, follows the empirical relationship given by Shin and Hahn [28], and that it is valid for epoxy in both its powder and liquid form, as it is a quantity which is independent of volume. Similarly, it is assumed that the thermal conductivity of the fully sintered epoxy follows the empirical relationship given by Shin and Hahn [28] to describe the thermal conductivity as a function of temperature and DoC.

To the author's knowledge, no data is available for the thermal conductivity of epoxy powders, however, the thermal conductivity of polyamide powder, $\kappa_{r,pow}$ was reported to be 0.05 – 0.0913 W/m K [52,53]. Given that the bulk thermal conductivity of polyamide and epoxy is similar (0.15 – 0.25 W/m K), data for polyamide powder is judged to be a reasonable approximation. The transition from powder to liquid resin is described for thermal conductivity using the following expression,

$$\kappa_r = \kappa_{r,pow}\,\frac{\chi}{\chi_0} + \kappa_{r,liq}\left(1 - \frac{\chi}{\chi_0}\right) \tag{29}$$

Where χ is the void fraction of the powder as determined using Equation 1, and χ_0 is the initial void fraction of the powder.

An alternative to the above may be to use analytical models to determine the effective thermal conductivity of the epoxy powder. Several such models have been developed for porous solids [54]. These models are a function of void fraction and the thermal conductivities of the two

phases (i.e. epoxy powder and vacuum). These models return a range of thermal conductivities for epoxy powder from 0.041 W/m K to 0.083 W/m K, which overlaps with the range reported for polyamide powder. Note, this range was based on a void fraction of 0.503 and Shin and Hahn's empirical relationship for the thermal conductivity of epoxy [28] at 55°C.

The thermal properties used for epoxy in this study are summarised in Table A.4 in Appendix A. Supplementary material.

Characterisation of the fibre-bed was not within the scope of this project. For this reason, most of the fibre-bed properties have been taken from the literature. Properties for stitched uni-directional (UD) fabrics and stitched triaxial fabrics were used in this study. The triaxial fabrics are treated as 3 UD plies in series. Assuming that the thermal conductivity of a composite lamina is transversely isotropic, the model developed by Clayton [55] is used to describe the through-thickness thermal conductivity, $\kappa_{c,T}$ of the UD plies. Some authors have experimentally measured the through-thickness conductivity of dry fabric under vacuum [56,57]. For dry GF fabric, they measured through-thickness thermal conductivities of 0.1 – 0.2 W/m K, depending on the fibre architecture (i.e. stitched UD, plain weave, twill weave, etc.).

Some properties and parameters are required to describe the fibre-bed for the flow models also. The permeability of a fibre-bed can be modelled or measured experimentally, however, reported values can vary significantly. The Gebart model for a quadratic packing structure [58] is used to calculate the intra-tow permeability for all simulations presented here. Experimental values from the literature were used for the inter-tow permeabilities of stitched UD fabrics.

Table A.5 in Appendix A. Supplementary material compiles the fibre-bed properties, parameters, and models that are used for the process simulations.

Additional material properties are required for the bagging materials and the mould tooling. For simplicity, the bagging is treated as one layer and the values reported by Joshi et al. [59] are used (see Table A.6 in Appendix A. Supplementary material). The bagging layer thickness is assumed to be 1.5 mm.

2.7 Initial conditions

Table 2 summarises the initial conditions that are used for the process simulations. A 100-ply glass-fibre/epoxy-powder laminate is used as a case study for the simulations. The cured ply thickness (h_{ply}) of a thin laminate was measured experimentally. The initial FVF of the VBO prepreg is controlled during the prepregging process using automated powder deposition. In-plane resin flow is expected to be negligible during processing, so it is assumed that the final FVF is approximately the same as the initial FVF i.e. no significant resin bleeding. An initial DoI of 0.113 is chosen based on experimental fitting detailed in Part II of this study [34]; this equates to a quarter of the available inter-tow space being filled during the powder deposition process. It is assumed that the epoxy powder is brought above its T_g during the prepregging process so that it adheres to the fibre-bed, but still retains its powder form. It is assumed that this prepregging process has a negligible effect on the DoC and there are negligible out-time effects between prepregging and laminate processing. For initialising the heat transfer model, this study assumed a uniform DoC (α) and temperature throughout the thick laminate. Based on real-world observations of vacuum bagged parts, an applied pressure of 90×10^3 Pa (90 kPa) is used for simulating laminate manufacture; it has been shown that deficient pressure conditions commonly occur and can be an important factor in VBO processing [43].

Table 2. Initial conditions used for the process simulations.

Parameter [units]	Value
No. of plies, N_p	100
Cured ply thickness, h_{ply} [mm]	1.0
Fibre volume fraction, V_f	0.5
Degree of impregnation, β	0.113

Powder void fraction, χ_0	0.485
Degree of cure, α	0.01
Applied pressure, P_{app} [Pa]	90×10^3
Laminate/bagging/tool temperature [°C]	23

2.8 Numerical computation

The finite difference code is run in MATLAB R2015a. To simulate the processing of a thick-section laminate, the laminate is discretized through the thickness, and the process models are numerically solved at the nodes. Many explicit and implicit finite difference methods exist for solving the heat equation, however, as previously indicated, an explicit forward time, central space scheme is used in this work. This is a first-order scheme, so it has limited accuracy (due to a large temporal truncation error), however, it is very simple to implement and is stable if the following criterion is met [48,60],

$$\gamma \frac{\Delta t}{\Delta z^2} < \frac{1}{2} \tag{30}$$

Where γ is the thermal diffusivity [m^2/s],

$$\gamma = \frac{\kappa}{\rho c_P} \tag{31}$$

Similarly, the Euler method is implemented for solving any ordinary differential equations (ODEs) in the simulation (e.g. cure kinetics, resin flow, etc.). Again, this is an explicit first order method which is simple to implement but has limited accuracy.

The number of nodes, N_n is based on the number of plies i.e,

$$N_n = N_p + 1 \tag{32}$$

The thermal diffusivity of the laminate, as well as that of the bagging and tooling, must be considered when choosing the maximum allowable time step size for a simulation. In cases where aluminium or steel tooling is used, the thermal diffusivity of the tooling is much higher than the composite material itself and limits the time step size. The maximum allowable time step size for a 1 mm thick ply of GF/Epoxy-powder is approximately 2.80 s (see Figure A.1 in Appendix A. Supplementary material), while it is 0.57 s for a 10 mm aluminium tool, and 3.55 s for a 10 mm steel tool. For a small enough time step, first order methods provide sufficient

accuracy due to the low rates of change associated with manufacturing thick-section composites i.e. slow ramp rates are used. As such, a time step of 0.5 s is chosen for all simulations using an aluminium tool, while a time step of 2.5 s is chosen for all simulations using a steel tool. Simulations show that there is no loss of accuracy when increasing from 0.5 s to 2.5 s increments for a steel tool (see Figure A.2 in Appendix A. Supplementary material).

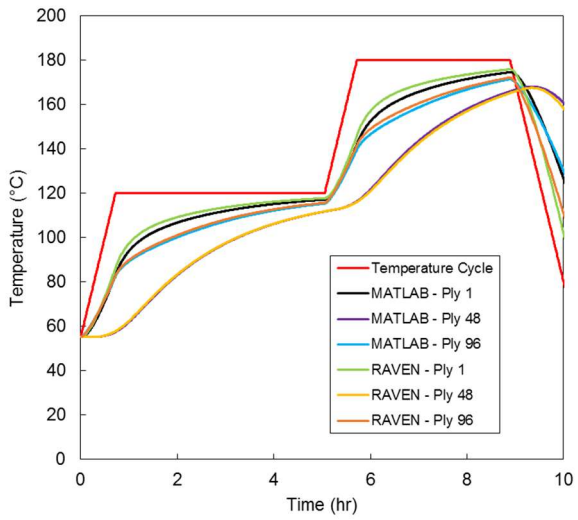

Figure 5. Comparison of the results from RAVEN and from the finite difference code developed in MATLAB. The simulations were carried out for a 96-ply GF/Epoxy-powder laminate heated on a 10 mm steel plate in an oven.

As a final verification of the numerical methods, the solution of the finite difference code is compared with results from RAVEN, a commercially available software for performing 1D heat transfer and cure kinetics simulations on composite laminates. Figure 5 shows that there is little difference between the solutions (< 5°C at any time). The simulations did not include compaction due to resin flow because it was not a featured capability of RAVEN. Furthermore, cure kinetics were excluded as it was not possible to implement a user-defined cure kinetics model in RAVEN which could simulate the cure kinetics of the GRN 918 epoxy powder.

3. Results and discussion

3.1 Powder sintering model

Figure 6 shows the results of the powder sintering model compared to the experimental data; converted from sample thickness to powder void fraction via Equations 2 and 3. As can be seen, Equation 1 is relatively accurate in describing the sintering behaviour of the GRN 918 powder. The sintering process corresponded to a 50% reduction of the powder sample's thickness. This highlighted that using epoxy powder would significantly increase the initial thickness of a composite preform compared to liquid epoxy.

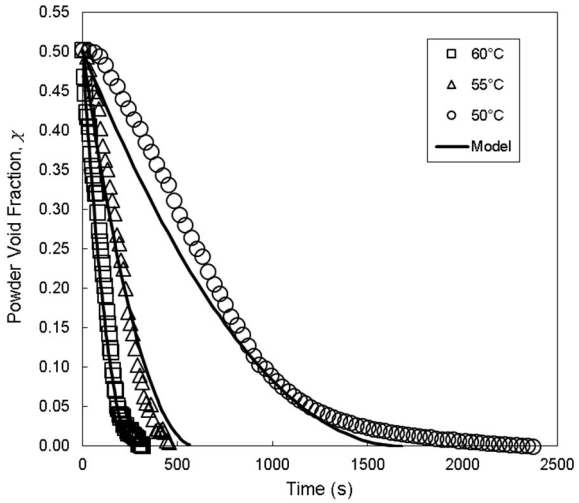

Figure 6. Results of the sintering model and experimental data for GRN 918.

Discrepancies between the data and model could be a result of the experimental set-up, which relied upon one-sided heating and an insulating sample hood. Use of a full environmental chamber may have given better temperature control, but it was unavailable at the time of testing. Another limitation of the test results was that the applied pressure was 52 kPa rather than 101.35 kPa (i.e. it was roughly half the pressure that would be expected for VBO processing). As such, the relationship of applied pressure and rate of sintering is not fully understood, and an improvement would be to repeat tests under various levels of applied pressure and determine if there is any significant effect.

3.2 Case study – Oven processing of a 100-ply laminate

As a starting point for investigating thick-section processing, the standard manufacturing process for a 100-ply laminate was considered. A thick-section laminate of GF/Epoxy-powder may be processed on a heated tool or in an oven using an extended version of the standard temperature cycle used for thin laminates i.e. with longer isothermal dwells to allow heat to transfer through all the plies. For this case study, the simulations focussed on a laminate being processed in an oven, on a steel plate with one layer of vacuum bagging around it.

The following temperature cycle was used:

- Drying stage: Ramp to 55°C and hold for 900 min
- Impregnation stage: Ramp to 120°C at 1.5°C/min and hold for 360 min
- Cure stage: Ramp to 180°C at 1.5°C/min and hold for 200 min
- Cool down

3.3 Temperature profile

Figure 7 shows how the temperature is predicted to evolve within the laminate with respect to time. Despite having symmetric thermal BCs, the temperatures at the bottom and top of the laminate (Ply 1 and Ply 100, respectively) are asymmetric because of the presence of the tool and bagging. During the drying stage (0 – 15 hr), the temperature at the centre of the laminate lags behind the outside of the laminate significantly. Heat transfer improves as the epoxy powder sinters, and the temperature of the laminate is predicted to approach the programmed temperature due to a small amount of exothermic heat being generated by the curing reaction (i.e. the DoC increases to approximately 0.2 during the drying stage; see Figure 8). The rate of heat transfer improves during the impregnation stage (15 – 22 hr), and again during the cure stage (22 – 26 hr). This is due to the increasing thermal diffusivity of the material as the laminate compacts and the thermal properties of the resin changes w.r.t. temperature and DoC; see Figure A.3, Figure A.4, and Figure A.5 in Appendix A. Supplementary material for plots of specific heat capacity, density and thermal conductivity, respectively. Naturally, the density of the laminate increases as the powder sinters and the fabric is impregnated. The thermal conductivity is influenced by these processes also due to the difference in thermal conductivities for powder vs fully sintered resin (ratio of approximately 1:2) and dry GF fabric vs fully impregnated GF fabric (ratio of approximately 1:1.3) – note, these ratios are

representative and assume ambient temperature and no curing. There is no thermal overshoot predicted for the laminate during the cure stage (i.e. above 120°C) due to GRN 918's low enthalpy of reaction. Conversely, the heat that is generated during the curing reaction aids heat transfer and allows the laminate to approach the programmed temperature, as previously mentioned for the drying cycle.

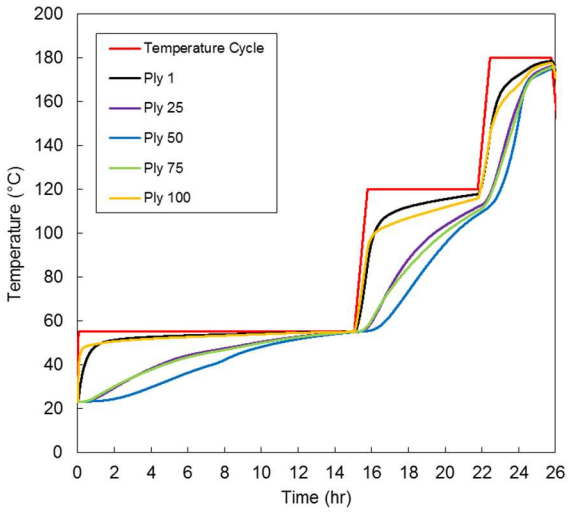

Figure 7. Plot of simulated ply temperatures within a 100-ply laminate. There is no temperature overshoot predicted, however, large thermal gradients are still present.

3.4 Cure profile

It has been demonstrated previously that GRN 918 epoxy powder can maintain a very low rate of cure up to 120°C due to the use of latent curing agents; allowing sufficient time for fabric impregnation to occur [8]. Despite this, the drying temperature (55°C) for the standard processing cycle is higher than the T_g of GRN 918 powder (approximately 40°C), resulting in increased molecular mobility for the epoxy. As such, Figure 8 shows that the simulations predict a slow increase in DoC during the drying stage. The rate of curing increases during the impregnation stage as the temperature increases, however, none of the plies are predicted to reach the gel point of the epoxy (i.e. DoC = 0.56) prior to the cure stage. Upon heating past 120°C, the DoC increases rapidly as the latent curing agent is activated. The entire laminate is predicted to reach a DoC > 0.9 within the first 3 hr of the cure stage, which is approximately

15% of the total processing cycle time (the impregnation stage accounts for approximately 27%, and the drying stage accounts for approximately 58%).

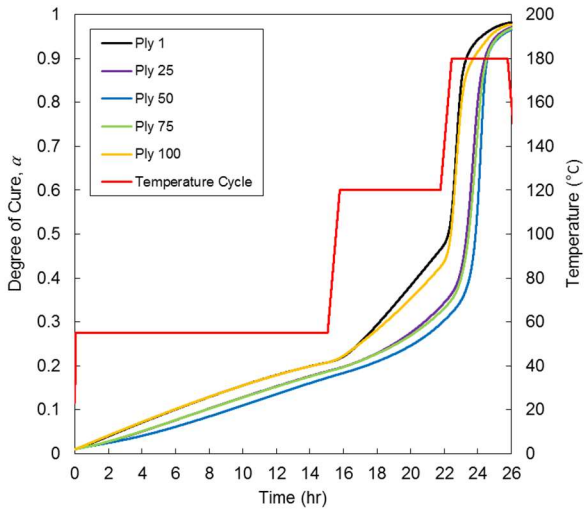

Figure 8. Plot of the simulated DoC evolution within the laminate.

3.5 Powder sintering, resin flow, and thickness change

An additional consequence of drying the powder above its T_g is that the powder is predicted to melt and sinter as the viscosity of the epoxy resin decreases (see Figure 9). This is beneficial for heat transfer in the laminate because fully sintered polymers have a higher thermal conductivity than polymer powders. On the other hand, dynamic vapour sorption (DVS) analysis has shown that powder sintering negatively affected the desorption properties of the epoxy [61]. By sintering the powder, moisture can no longer desorb from the surface of the powder particle and must diffuse through the bulk polymer. Furthermore, the powder acts as permeable layer through which gases can be evacuated, whereas the sintered epoxy forms a barrier and the gases must pass through the dry fibre tows; similar to conventional VBO prepregs [38,62].

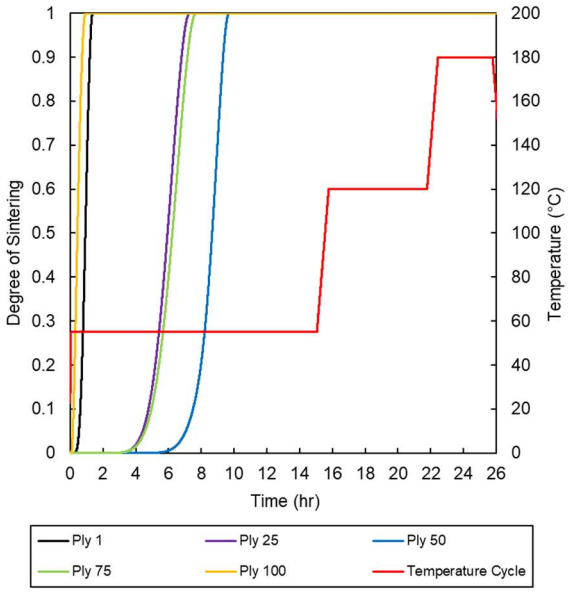

Figure 9. Powder sintering during the drying stage.

The sintering process also results in a significant decrease in the laminate thickness; approximately 26% as shown in Figure 10. Ideally, a shortened drying stage would be carried out below the T_g of the epoxy powder (due to the advantageous sorption properties of the powder), and then an additional stage at an intermediate temperature could be introduced to promote powder sintering and improve heat transfer within the laminate. To optimise the drying stage in this way, more research is required which is outside the scope of this work.

After the drying stage, the remaining thickness reduction predicted (19%) in Figure 10 is due to resin flow; in total the laminate thickness decreases by approximately 45%. As shown in Figure 11, the simulation predicts that the inter-tow region (DoI < 0.45) would fill during the drying stage when powder has sintered and reaches a sufficiently low viscosity to flow between the tows. For the outer plies, it is predicted that the inter-tow region would be completely filled within the first few hours of the temperature cycle, however, the inner plies lag by several hours due to slow heat transfer. The timescale for this process confirms the need to model inter-tow flow for the current material system. In contrast, intra-tow filling (DoI > 0.45) is relatively fast when the resin viscosity is sufficiently low (see Figure 12 for the viscosities).

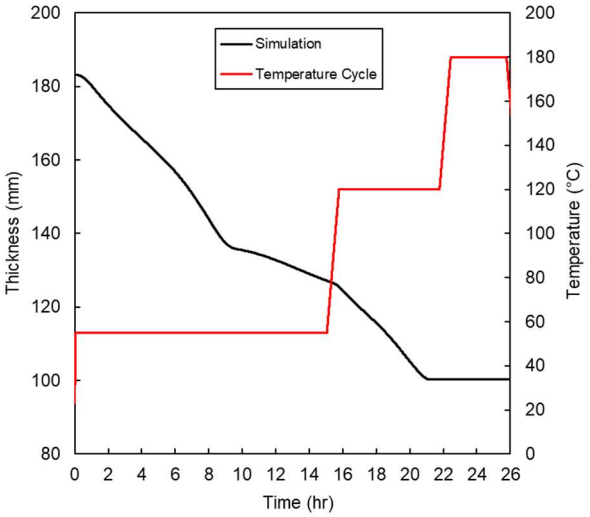

Figure 10. The thickness change plot of the GF/Epoxy-powder laminate during the temperature cycle. A large reduction in thickness is predicted during the drying stage due to the sintering of the powder. After the cessation of sintering, the resin is predicted to slowly flow into and fill the inter-tow region of the fibre-bed. During the impregnation stage, the viscosity of the resin reduces, the resin fills the fibre tows, and the laminate thickness decreases again.

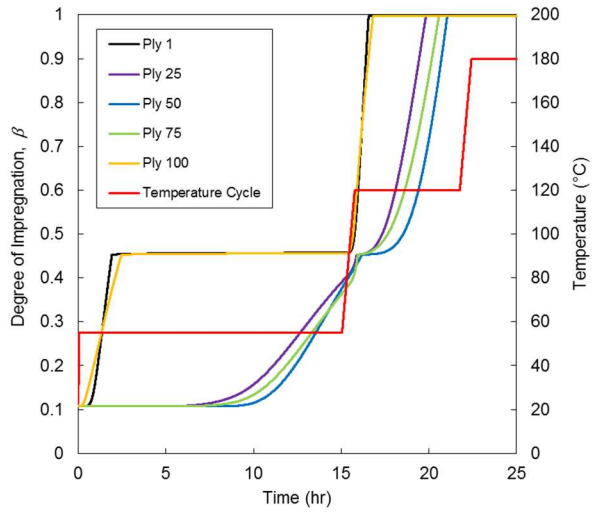

Figure 11. Plot of the degree of impregnation during the simulated temperature cycle. The inter-tow region (DoI < 0.45) fills during the drying cycle, but lower viscosities are required for filling the fibre tows (DoI > 0.45).

It is noted that the simulated viscosities in Figure 12 are relatively high for GF fabric impregnation, however, additional calculations using the analytical solution described by Cender et al. [19] confirms that, even for a resin viscosity of 1000 Pa s, a ply could be fully impregnated within 80 mins. Whether this is true remains unclear, as other factors can inhibit

the completion of filling (e.g. pressure sharing of the fibre-bed, pressure deficient conditions, etc.).

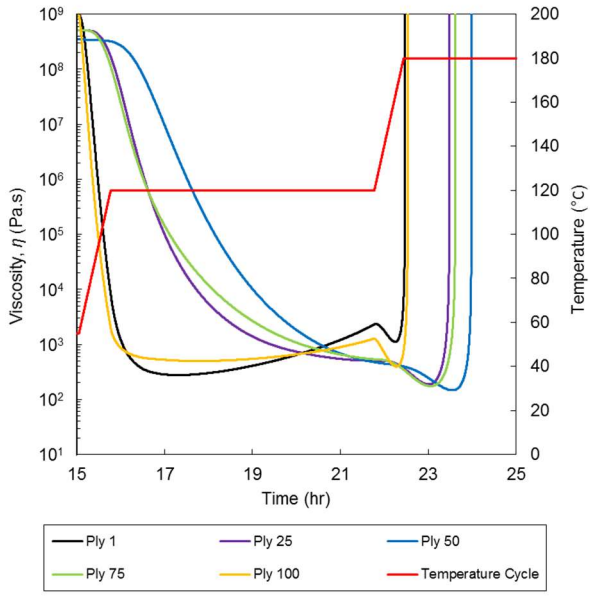

Figure 12. Plot of the resin viscosity during the impregnation and cure stages of the temperature cycle (note the reduced time span on the horizontal axis). The viscosities are predicted to drop significantly when the temperature is increased to 120°C. Upon heating above 120°C, the epoxy reaches its gel point, and the viscosity tends towards infinity.

4. Conclusions

The development of 1D numerical models for manufacturing thick-section composites using powder-based VBO prepregs has been described. This includes process models for coupled resin flow and heat transfer within VBO prepregs, and material models specifically developed for an epoxy powder system. Using first order numerical methods, it was possible to solve these models for a typical composites temperature cycle. The accuracy of the heat transfer model was verified by comparing the results of the code to results from the commercial composite processing software, RAVEN. Due to limitations with RAVEN, it was not possible to verify or validate the cure kinetics model, resin flow model, or powder sintering model. Validation experiments for these models are the subject of concurrent work (Part II [34]).

A case study was carried out on a 100-ply laminate which was processed in an oven on steel tooling. The study was used to demonstrate the capability of the numerical models and to

analyse a typical temperature cycle used by industry for manufacturing thick-section composite parts. For the drying stage, it was found that the current drying temperature was high enough to melt and sinter the powder throughout the laminate. This plays an important role in improving heat transfer within the laminate but may not be efficient in terms of drying the epoxy. With more analysis and modelling of moisture desorption and gas evacuation, it would possible to optimise the drying stage of the temperature cycle, however, this was outside the scope of this work.

An existing dual-scale resin flow model for VBO prepreg was used as the basis of the resin flow in this system. This dual-scale model simulated resin flow around the fibre tows (inter-tow) and into the fibre tows (intra-tow). It was found that the resin viscosity profile varied significantly depending on the resin's position within the laminate. Due to the advancement of cure, the resin viscosity did not reach below 100 Pa s, however, the resin flow model still predicted that the fibre-bed would reach full impregnation during the 120°C dwell. The fabric impregnation, along with powder sintering, contributed to a 45% reduction in the thickness of the laminate. This thickness change was computed based on a simplified microstructural model which required values for the cured ply thickness, the intra-tow porosity, and the fibre volume fraction of an individual ply. This microstructural model also played a role in coupling resin flow to the heat transfer model by updating each ply's thickness, and thermal properties.

Simulated temperature profiles for the 100-ply laminate showed that heat transfer improved over the duration of the processing cycle. Powder sintering and fabric impregnation contributed to increases in thermal conductivity. Temperature-dependent and cure-dependent material properties were taken from the literature; these contributed to improved heat transfer also, especially during the cure stage. The low enthalpy of reaction for GRN 918 epoxy powder meant that there was no significant build-up of heat predicted in the laminate and subsequently no overshoot in temperature, thus eliminating the risk of thermal runaway.

Acknowledgements

The authors acknowledge financial support from MARINCOMP, "Novel Composite Materials & Processes for Marine Renewable Energy", a European Union Marie Curie FP7 Project funded under the IAPP call (Grant No. 612531), the Institute of Materials and Processes at the University of Edinburgh, industrial partners Suzlon Energy Limited (NL Branch), Johns Manville, and ÉireComposites Teo. We also acknowledge funding from POWDERBLADE,

"Commercialisation of Advanced Composite Material Technology: Carbon-Glass Hybrid in Powder Epoxy for Large Wind Turbine Blades", Funded under: European Union Horizon 2020, Fast Track to Innovation Pilot, Grant No. 730747. We would also like to acknowledge the Composites Manufacturing and Simulation Center at Purdue University for the use of RAVEN software.

Nomenclature [units]

α	Degree of cure
β	Degree of impregnation
γ	Thermal diffusivity [m^2/s]
η	Viscosity [Pa s]
κ	Thermal conductivity [W/m K]
$\kappa_{c,T}$	Transverse thermal conductivity of the impregnated composite [W/m K]
κ_{fab}	Thermal conductivity of the dry fabric [W/m K]
κ_r	Thermal conductivity of the epoxy [W/m K]
$\kappa_{r,liq}$	Thermal conductivity of the liquid epoxy [W/m K]
$\kappa_{r,pow}$	Thermal conductivity of the epoxy powder [W/m K]
ρ	Density [kg/m^3]
ρ_0	Initial density of the powder [kg/m^3]
ρ_c	Composite density [kg/m^3]
ρ_f	Fibre density [kg/m^3]
ρ_P	Bulk polymer density [kg/m^3]
ρ_r	Resin density [kg/m^3]
φ	Total porosity/resin volume fraction
φ_1	Inter-tow porosity
φ_2	Intra-tow porosity
φ_{fab}	Porosity of the fabric layer
χ	Powder void fraction during sintering
χ_0	Initial powder void fraction of the powder
χ_E	Pre-exponential rate constant for sintering
χ_∞	Final powder void fraction during sintering
A_{ell}	Area of an ellipse [m^2]
A_{rec}	Area of a rectangle [m^2]
B	Fitting constant
c_P	Specific heat capacity [J/kg K]
$C_{\chi 1}$	Fitting constant for sintering model
$C_{\chi 2}$	Fitting constant for sintering model [K]
h	Heat transfer coefficient [W/m^{2}K]
h_{fab}	Thickness of the fabric layer [m]
h_{lam}	Total laminate thickness [m]
h_{ply}	Thickness of a fully impregnated ply (cured ply thickness) [m]
h_r	Thickness of resin layer [m]
H_T	Total enthalpy of reaction [J/g]
i	Time step for finite difference code
j	Through-thickness nodal position for finite difference code
K	Permeability [m^2]
K_1	Inter-tow permeability [m^2]
K_2	Intra-tow permeability [m^2]
L	Thickness of sintered powder samples [m]
L_0	Initial thickness of powder samples [m]
L_1	Characteristic length of the inter-tow porous medium [m]
l	Resin flow front distance from the inlet [m]
l_{bot}	Resin flow front distance from the bottom of the fabric layer [m]
l_{top}	Resin flow front distance from the top of the fabric layer [m]
l_{tot}	Total impregnation depth [m]
m_r	Resin mass fraction
N_n	Number of nodes

N_p	Number of plies	
P	Pressure [Pa]	
P_{app}	Applied pressure [Pa]	
$R_{j,j-1}$	Thermal resistance of material between nodes j and $j-1$ [m^{2}K/W]	
$R_{j+1,j}$	Thermal resistance of material between nodes $j+1$ and j [m^{2}K/W]	
T	Temperature [K]	
$T_{i,s}$	Surface temperature at time step i [K]	
$T_P(i)$	Programmed temperature at time step i [K]	
T_θ	Onset temperature for melting [K]	
t	Time [s]	
Δt	Time step size for finite difference code [s]	
V_f	Fibre volume fraction	
x	Flow direction	
Δz	Element thickness of node j [m]	

References

[1] Price RV. Production of Impregnated Rovings. 3742106, 1973.

[2] Edie D., Lickfield GC, Allen LE, McCollum JR. Thermoplastic Coating of Carbon Fibres. Hampton, VA, USA: 1989.

[3] Baucom RM, Marchello JM. Powder towpreg process development. Proc. NASA Adv. Compos. Technol. Conf., 1990, p. 443–54.

[4] Bayha TD, Osborne PP, Thrasher TP, Hartness JT, Johnston NJ, Marchello JM, et al. Processing, Properties and Applications of Composites Using Powder-Coated Epoxy Towpreg Technology. Proc. NASA's 4th Adv. Compos. Technol. Conf., Salt Lake City, Utah: 1993.

[5] Stone KR, Springer JJ. Advanced Composites Technology Case Study at NASA Langley Research Center. 1995.

[6] Ó Brádaigh CM, Doyle A, Doyle D, Feerick PJ. Electrically-Heated Ceramic Composite Tooling for Out-of-Autoclave Manufacturing of Large Composite Structures. SAMPE J 2011;47.

[7] Robert C, Mamalis D, Alam P, Lafferty AD, Ó Cadhain C, Breathnach G, et al. Powder Epoxy Based UD-CFRP Manufacturing Routes For Turbine Blade Application. Proc. SAMPE Eur. Conf. '18, Southampton, UK: 2018.

[8] Maguire JM, Nayak K, Ó Brádaigh CM. Characterisation of epoxy powders for processing thick-section composite structures. Mater Des 2018;139:112–21. https://doi.org/10.1016/J.MATDES.2017.10.068.

[9] Mamalis D, Flanagan T, Ó Brádaigh CM. Effect of fibre straightness and sizing in carbon fibre reinforced powder epoxy composites. Compos Part A Appl Sci Manuf 2018;110:93–105. https://doi.org/https://doi.org/10.1016/j.compositesa.2018.04.013.

[10] Murray JJ, Pappa EJ, Mamalis D, Breathnach G, Doyle A, Flanagan T, et al. Characterisation of carbon fibre reinforced powder epoxy composites for wind energy blades. Proc. 18th Eur. Conf. Compos. Mater., Athens, Greece: 2018.

[11] Mamalis D, Murray JJ, McClements J, Tsikritsis D, Koutsos V, McCarthy ED, et al. Novel carbon-fibre powder-epoxy composites: Interface phenomena and interlaminar fracture behaviour. Compos Part B Eng 2019:107012. https://doi.org/10.1016/J.COMPOSITESB.2019.107012.

[12] Ramasamy A, Wang Y, Muzzy J. Braided thermoplastic composites from powder-coated towpregs. Part I: Towpreg characterization. Polym Compos 1996;17:497–504. https://doi.org/https://doi.org/10.1002/pc.10639.

[13] Bogetti TA, Gillespie JW. Two-Dimensional Cure Simulation of Thick Thermosetting Composites. J Compos Mater 1991;25:239–73. https://doi.org/https://doi.org/10.1177/002199839102500302.

[14] Advani SG, Hsiao K-T. 1 – Introduction to composites and manufacturing processes. Manuf. Tech. Polym. Matrix Compos., Woodhead Publishing Limited; 2012, p. 1–12. https://doi.org/https://doi.org/10.1533/9780857096258.1.1.

[15] Darcy H. Les fontaines publiques de la ville de Dijon. Paris, France: 1856.

[16] Celle P, Drapier S, Bergheau J-M. Numerical modelling of liquid infusion into fibrous media undergoing compaction. Eur J Mech - A/Solids 2008;27:647–61. https://doi.org/10.1016/j.euromechsol.2007.11.002.

[17] Merotte J, Simacek P, Advani SG. Resin flow analysis with fiber preform deformation in through thickness direction during Compression Resin Transfer Molding. Compos Part A Appl Sci Manuf 2010;41:881–7. https://doi.org/10.1016/j.compositesa.2010.03.001.

[18] Centea T, Hubert P. Modelling the effect of material properties and process parameters on tow impregnation in out-of-autoclave prepregs. Compos Part A Appl Sci Manuf 2012;43:1505–13. https://doi.org/https://doi.org/10.1016/j.compositesa.2012.03.028.

[19] Cender TA, Simacek P, Advani SG. Resin film impregnation in fabric prepregs with dual length scale permeability. Compos Part A Appl Sci Manuf 2013;53:118–28. https://doi.org/https://doi.org/10.1016/j.compositesa.2013.05.013.

[20] Kuentzer N, Simacek P, Advani SG, Walsh S. Permeability characterization of dual scale fibrous porous media. Compos Part A Appl Sci Manuf 2006;37:2057–68. https://doi.org/https://doi.org/10.1016/j.compositesa.2005.12.005.

[21] Zhou F, Kuentzer N, Simacek P, Advani SG, Walsh S. Analytic characterization of the

permeability of dual-scale fibrous porous media. Compos Sci Technol 2006;66:2795–803. https://doi.org/https://doi.org/10.1016/j.compscitech.2006.02.025.

[22] Loos AC, Springer GS. Curing of Epoxy Matrix Composites. J Compos Mater 1983;17:135–69. https://doi.org/https://doi.org/10.1177/002199838301700204.

[23] Martinez GM. FAST CURES FOR THICK LAMINATED ORGANIC MATRIX COMPOSITES. Chem Eng Sci 1990;46:439–50. https://doi.org/https://doi.org/10.1016/0009-2509(91)80005-J.

[24] Lee S-Y, Springer GS. Filament Winding Cylinders I. Process Model. J Compos Mater 1990;24:1270–98. https://doi.org/https://doi.org/10.1177/002199839002401202.

[25] Twardowski TE, Lin SE, Geil PH. Curing in Thick Composite Laminates: Experiment and Simulation. J Compos Mater 1993;27:216–50. https://doi.org/https://doi.org/10.1177/002199839302700301.

[26] Shi L. Heat Transfer in the Thick Thermoset Composites. PhD Thesis, Technische Univeristeit Delft, 2016.

[27] Oh JH, Lee DG. Cure Cycle for Thick Glass/Epoxy Composite Laminates. J Compos Mater 2002;36:19–45. https://doi.org/https://doi.org/10.1177/0021998302036001300.

[28] Shin DD, Hahn HT. Compaction of Thick Composites: Simulation and Experiment. Polym Compos 2004;25:49–59. https://doi.org/https://doi.org/10.1002/pc.20004.

[29] Maguire JM, Ó Brádaigh CM, Simacek P, Advani SG. Through thickness resin flow and heat transfer modelling of partially impregnated composite materials for thick-section parts. 13th Int. Conf. Flow Process. Compos. Mater., Kyoto, Japan: 2016.

[30] Maguire JM, Doyle A, Ó Brádaigh CM. Process modelling of thick-section tidal turbine blades using low-cost fibre reinforced polymers. 12th Eur. Wave Tidal Energy Conf., Cork, Ireland: 2017.

[31] Greco A, Maffezzoli A. Polymer Melting and Polymer Powder Sintering by Thermal Analysis. J Therm Anal Calorim 2003;72:1167–74. https://doi.org/https://doi.org/10.1023/A:1025096432699.

[32] Frenkel J. Viscous Flow of Crystalline Bodies under the Action of Surface Tension. J Phys (U S S R) 1945;9:385–91.

[33] Kandis M, Bergman TL. Observation, Prediction, and Correlation of Geometric Shape Evolution Induced by Non-Isothermal Sintering of Polymer Powder. J Heat Transfer 1997;119:824–31. https://doi.org/https://doi.org/10.1115/1.2824189.

[34] Maguire JM, Nayak K, Ó Brádaigh CM. Novel epoxy powder for manufacturing thick-section composite parts under vacuum-bag-only conditions. Part II: Experimental

validation and process investigations. Compos Part A Appl Sci Manuf 2020;In review.
[35] ÉireComposites Teo. GRN 918 Datasheet. 2013.
[36] Khoun L, Centea T, Hubert P. Characterization Methodology of Thermoset Resins for the Processing of Composite Materials -- Case Study: CYCOM 890RTM Epoxy Resin. J Compos Mater 2009;44:1397–415. https://doi.org/https://doi.org/10.1177/0021998309353960.
[37] Khoun L, Hubert P. Cure shrinkage characterization of an epoxy resin system by two in situ measurement methods. Polym Compos 2010;31:1603–10. https://doi.org/https://doi.org/10.1002/pc.20949.
[38] Cender TA, Simacek P, Davis S, Advani SG. Gas Evacuation from Partially Saturated Woven Fiber Laminates. Transp Porous Media 2016;115:541–62. https://doi.org/https://doi.org/10.1007/s11242-016-0784-x.
[39] Centea T, Grunenfelder LK, Nutt SR. A review of out-of-autoclave prepregs – Material properties, process phenomena, and manufacturing considerations. Compos Part A Appl Sci Manuf 2015;70:132–54. https://doi.org/https://doi.org/10.1016/j.compositesa.2014.09.029.
[40] Helmus R, Centea T, Hubert P, Hinterhölzl R. Out-of-autoclave prepreg consolidation: Coupled air evacuation and prepreg impregnation modeling. J Compos Mater 2016;50:1403–13. https://doi.org/https://doi.org/10.1177/0021998315592005.
[41] Wysocki M, Asp LE, Toll S, Larsson R. Two phase continuum modelling of composites consolidation. Plast Rubber Compos 2009;38:93–7. https://doi.org/10.1179/174328909X387856.
[42] Gangloff JJ, Simacek P, Sinha S, Advani SG. A process model for the compaction and saturation of partially impregnated thermoset prepreg tapes. Compos Part A Appl Sci Manuf 2014;64:234–44. https://doi.org/10.1016/j.compositesa.2014.05.010.
[43] Centea T, Hubert P. Out-of-autoclave prepreg consolidation under deficient pressure conditions. J Compos Mater 2013;48:2033–45. https://doi.org/https://doi.org/10.1177/0021998313494101.
[44] Tahir MW, Hallström S, Åkermo M. Effect of dual scale porosity on the overall permeability of fibrous structures. Compos Sci Technol 2014;103:56–62. https://doi.org/https://doi.org/10.1016/J.COMPSCITECH.2014.08.008.
[45] Amico S, Lekakou C. Flow through a Two-Scale Porosity, Oriented Fibre Porous Medium. Transp Porous Media 2004;54:35–53. https://doi.org/https://doi.org/10.1023/A:1025799404038.

[46] Loos AC, MacRae JD. A process simulation model for the manufacture of a blade-stiffened panel by the resin film infusion process. Compos Sci Technol 1996;56:273–89. https://doi.org/https://doi.org/10.1016/0266-3538(96)80008-X.
[47] Costa VAF, Sousa ACM. Modeling of flow and thermo-kinetics during the cure of thick laminated composites. Int J Therm Sci 2003;42:15–22. https://doi.org/https://doi.org/10.1016/S1290-0729(02)00003-0.
[48] Çengel YA. Heat Transfer – A Practical Approach. 2nd ed. New York, USA: McGraw-Hill; 2003.
[49] Zimmermann K, Van Den Broucke B. Assessment of process-induced deformations and stresses in ultra thick laminates using isoparametric 3D elements. J Reinf Plast Compos 2012;31:163–78. https://doi.org/https://doi.org/10.1177/0731684411433315.
[50] Monaghan PF, Brogan MT, Oosthuizen PH. Heat transfer in an autoclave for processing thermoplastic composites. Compos Manuf 1991;2:233–42. https://doi.org/https://doi.org/10.1016/0956-7143(91)90145-7.
[51] Kluge NEJ, Lundström TS, Ljung A-L, Westerberg LG, Nyman T. An experimental study of temperature distribution in an autoclave. J Reinf Plast Compos 2016;35:566–78. https://doi.org/https://doi.org/10.1177/0731684415624768.
[52] Xue S, Barlow JW. Thermal Properties of Powders. Proc. 1990 Int. Solid Free. Fabr. Symp., 1990, p. 179–85.
[53] Tian X, Peng G, Yan M, He S, Yao R. Process prediction of selective laser sintering based on heat transfer analysis for polyamide composite powders. Int J Heat Mass Transf 2018;120:379–86. https://doi.org/https://doi.org/10.1016/J.IJHEATMASSTRANSFER.2017.12.045.
[54] Smith DS, Alzina A, Bourret J, Nait-Ali B, Pennec F, Tessier-Doyen N, et al. Thermal conductivity of porous materials. J Mater Res 2013;28:2260–72. https://doi.org/10.1557/jmr.2013.179.
[55] Clayton WA. Constituent and composite thermal conductivities of phenolic-carbon and phenolic-graphite ablators. Proc. 12th Struct. Struct. Dyn. Mater. Conf., Anaheim, CA, USA: 1971, p. 19–21.
[56] El-Hage Y, Hind S, Robitaille F. Thermal conductivity of textile reinforcements for composites. J Text Fibrous Mater 2018;1:1–12. https://doi.org/https://doi.org/10.1177/2515221117751154.
[57] Lee C. An Investigation into the Transverse Thermal Conductivity of Fibre Beds. MEng Thesis, University of Limerick, 2004.

[58] Gebart BR. Permeability of Unidirectional Reinforcements for RTM. J Compos Mater 1992;26:1100–33. https://doi.org/https://doi.org/10.1177/002199839202600802.
[59] Joshi SC, Liu XL, Lam YC. A numerical approach to the modeling of polymer curing in fibre-reinforced composites. Compos Sci Technol 1999;59:1003–13. https://doi.org/https://doi.org/10.1016/S0266-3538(98)00138-9.
[60] Recktenwald GW. Finite-Difference Approximations to the Heat Equation. 2011.
[61] Maguire JM. Processing of Thick Section Epoxy Powder Composite Structures. PhD Thesis, The University of Edinburgh, 2019.
[62] Grunenfelder LK, Dills A, Centea T, Nutt S. Effect of prepreg format on defect control in out-of-autoclave processing. Compos Part A Appl Sci Manuf 2017;93:88–99. https://doi.org/https://doi.org/10.1016/J.COMPOSITESA.2016.10.027.
[63] Kenny JM, Opalicki M. Influence of the chemorheology of toughened epoxy matrices on the processing behavior of high performance composites. Makromol Chemie Macromol Symp 1993;68:41–56. https://doi.org/https://doi.org/10.1002/masy.19930680106.
[64] DiBenedetto AT. Prediction of the glass transition temperature of polymers: A model based on the principle of corresponding states. J Polym Sci Part B Polym Phys 1987;25:1949–69. https://doi.org/https://doi.org/10.1002/polb.1987.090250914.
[65] Ruiz E, Trochu F. Numerical analysis of cure temperature and internal stresses in thin and thick RTM parts. Compos Part A Appl Sci Manuf 2005;36:806–26. https://doi.org/https://doi.org/10.1016/j.compositesa.2004.10.021.
[66] Wieland B, Ropte S. Process Modeling of Composite Materials for Wind-Turbine Rotor Blades: Experiments and Numerical Modeling. Materials (Basel) 2017;10:1157–69. https://doi.org/https://doi.org/10.3390/ma10101157.
[67] Hsiao K-T, Laudorn H, Advani SG. Experimental Investigation of Heat Dispersion Due to Impregnation of Viscous Fluids in Heated Fibrous Porous During Composites Processing. J Heat Transfer 2001;123:178–87. https://doi.org/https://doi.org/10.1115/1.1338131.
[68] Tan H, Pillai KM. Multiscale modeling of unsaturated flow of dual-scale fiber preform in liquid composite molding II: Non-isothermal flows. Compos Part A Appl Sci Manuf 2012;43:14–28. https://doi.org/https://doi.org/10.1016/j.compositesa.2011.06.012.
[69] Johns Manville. Single-end Roving Selector Guide. 2018.
[70] Springer GS, Tsai SW. Thermal Conductivities of Unidirectional Materials. J Compos Mater 1967;1:166–73. https://doi.org/https://doi.org/10.1177/002199836700100206.

Appendix A. Supplementary material

Additional material models from Maguire et al. [8]

The viscosity, η, is described using the following WLF-type chemorheological model which was developed by Kenny & Opalicki [63] for toughened epoxy systems,

$$\eta = \eta_{g0}\ \exp\left(\frac{-C_{\eta 1}\left[T - T_g\right]}{C_{\eta 2} + T - T_g}\right)\left(\frac{\alpha_g}{\alpha_g - \alpha}\right)^A \tag{A.1}$$

Where η_{g0} is the viscosity of the uncured resin [Pa s] at the initial glass transition temperature, T_{g0} [K], α_g is the DoC at gelation, $C_{\eta 1}$, $C_{\eta 2}$ [K], and A are fitting constants. The cure-dependent glass transition temperature, T_g [K], was modelled using the DiBenedetto equation [64],

$$\frac{T_g - T_{g0}}{T_{g\infty} - T_{g0}} = \frac{\lambda\alpha}{1 - (1 - \lambda)\alpha} \tag{A.2}$$

Where T_{g0} is the initial glass transition temperature of the uncured resin [K], $T_{g\infty}$ is the glass transition temperature of the fully cured resin [K], and λ is a fitting constant.

The viscosity couples the resin flow model to the heat transfer and cure kinetics models via the temperature dependency and DoC dependency, respectively. The following cure kinetics model was developed for GRN 918 [8],

$$\frac{d\alpha}{dt} = \frac{(k_{\alpha 1} + k_{\alpha 2} + k_{\alpha 3}\alpha^m)(1 - \alpha)^n}{1 + \exp[C(\alpha - \alpha_c)]} \tag{A.3}$$

Where $k_{\alpha 1}$, $k_{\alpha 2}$, and $k_{\alpha 3}$ are cure rate constants [s^{-1}], m and n are the reaction orders, C is a diffusion constant, and α_c is the temperature-dependent critical DoC, above which the reaction becomes diffusion-controlled.

The fitting parameters for Equations A.1, A.2, and A.3 are given in Table A.1, Table A.2, and

Table A.3 respectively.

Table A.1. Chemorheological model parameters for GRN 918 epoxy powder.

Parameter [units]	Value
η_{g0} [Pa s]	2×10^{11}
$C_{\eta 1}$	32.25
$C_{\eta 2}$ [K]	30
α_g	0.56
A	1.6

$$\eta = \eta_{g0} \exp\left(\frac{-C_{\eta 1}[T - T_g]}{C_{\eta 2} + T - T_g}\right)\left(\frac{\alpha_g}{\alpha_g - \alpha}\right)^A$$

Table A.2. Parameters for the DiBenedetto model.

Parameter [units]	Value
T_{g0} [°C]	40
$T_{g\infty}$ [°C]	106
λ	0.53

$$\frac{T_g - T_{g0}}{T_{g\infty} - T_{g0}} = \frac{\lambda\alpha}{1 - (1 - \lambda)\alpha}$$

Table A.3. Fitted cure kinetics parameters for GRN 918 epoxy powder.

Parameter [units]	Value	Parameter [units]	Value
$A_{\alpha 1}$ [s^{-1}]	4.073×10^{-4}	m	1.24
$E_{\alpha 1}$ [J/mol]	12006	n	1.8
$A_{\alpha 2}$ [s^{-1}]	10.112×10^{9}	C	50
$E_{\alpha 2}$ [J/mol]	111792	α_c	$0.006\,T$ - 1.748
$A_{\alpha 3}$ [s^{-1}]	1.636×10^{13}		
$E_{\alpha 3}$ [J/mol]	131240		
$\frac{d\alpha}{dt} = \frac{(k_{\alpha 1} + k_{\alpha 2} + k_{\alpha 3}\alpha^m)(1-\alpha)^n}{1+\exp[C(\alpha-\alpha_c)]}$, $k_{\alpha i} = A_{\alpha i}\exp\left(\frac{-E_{\alpha i}}{RT}\right)$, $i = 1,2,3$			

Derivation of the pressure boundary condition at the interface of two porous media

For intra-tow flow, the pressure boundary condition at the interface of the two porous media P_{L1} must be derived. Assuming mass conservation for resin flow through the porous media,

$$\frac{du}{dx} = 0 \tag{A.4}$$

Then,

$$\frac{-K_1(P_{app} - P_{L1})}{\eta L_1} = \frac{-K_2(P_{L1} - P_f)}{\eta(l - L_1)} \tag{A.5}$$

Where P_f is the pressure at the flow front (assumed to be zero under vacuum conditions). As such, the equation reduces to:

$$P_{L1} = \frac{K_1 P_{app}(l - L_1)}{K_2 L_1 + K_1(l - L_1)} \tag{A.6}$$

1

2 Rule of mixtures equations for the heat transfer model

3 A rule of mixtures approach was implemented by several authors for describing the composite
4 density and specific heat capacity within the heat equation [22,23,49,59,65,66]:

$$\rho_c = \rho_f V_f + \rho_r(1 - V_f) \tag{A.7}$$

$$c_{P,c} = \frac{c_{P,f}\rho_f V_f + c_{P,r}\rho_r(1 - V_f)}{\rho_f V_f + \rho_r(1 - V_f)} \tag{A.8}$$

5 Where V is the volume fraction, and subscripts f and r denote fibre and resin, respectively.

6

7 Equations for heat transfer through the bagging or tooling

8 Heat transfer at the boundary of the laminate and bagging was written as,

$$\left(\Delta z \rho c_P \frac{dT}{dt}\right)_{i,B} = \left(\frac{T_{j-1} - T_B}{R_{B,j-1}} + \frac{T_B - T_{B+1}}{R_{B+1,B}}\right)_i + \left(z_r \rho_r (1 - V_f) H_T \frac{d\alpha}{dt}\right)_{i,B} \tag{A.9}$$

9 Where subscript B represents the node at the boundary and is equivalent to node j in the
10 laminate. Note that the above can be easily written for the boundary of the laminate and tooling
11 by changing the subscripts appropriately.

12 The average spatial difference, Δz, was approximated by,

$$\Delta z_{(i,B)} = \frac{2h_{r(i,j)} + h_{fab} + 2z_{bt}}{2} \tag{A.10}$$

13 Where z_{bt} is the spatial increment size for the bagging/tooling, represented by,

$$z_{bt} = \frac{h_{bt}}{N - 1} \tag{A.11}$$

14 Where h_{bt} is the total thickness of the bagging/tooling, and N is the total number of nodes for
15 the discretised bagging/tooling.

16 The combined density and specific heat capacity at the boundary node were approximated
17 using a rule of mixtures approach,

$$\rho_{(i,B)} = \frac{\rho_{bt} z_{bt} + \rho_j (h_{r(i,j)} + h_{fab}/2)}{\Delta z_{(i,B)}} \quad \text{(A.12)}$$

$$c_{P,B} = \frac{c_{P,bt}\rho_{bt} z_{bt} + c_{P(i,j)}\rho_{(i,j)} (h_{r(i,j)} + h_{fab}/2)}{\rho_{bt} z_{bt} + \rho_{(i,j)} \left(h_{r(i,j)} + h_{fab}/2\right)} \quad \text{(A.13)}$$

Where the subscript bt refers to bagging/tooling.

The thermal resistance, $R_{B,j-1}$, was taken to be equivalent to $R_{j,j-1}$ (Equation 24). If the thermal conductivity and thickness of each bagging layer is known, a full thermal resistance term can be deduced. For this work, however, $R_{B+1,B}$ was simply written as,

$$R_{B+1,B} = \frac{z_{bt}}{\kappa_{bt}} \quad \text{(A.14)}$$

Where κ_{bt} was a lumped thermal conductivity for the whole bagging layer.

Properties and parameters used in the process models

Table A.4. Thermal properties used to model heat transfer in GRN 918.

Property [units]	**Value**	**Source**
Specific heat capacity of epoxy, $c_{P,r}$ [J/kg °C]*	Equation A.15	[28]
Thermal conductivity of liquid epoxy, $\kappa_{r,liq}$ [W/m °C]*	Equation A.16	[28]
Thermal conductivity of powder epoxy, $\kappa_{r,pow}$ [W/m K]	0.075**	-

$$c_{P,r} = 4184(0.468 + 5.975 \times 10^{-4} T - 0.141\alpha) \quad \text{(A.15)}$$

$$\kappa_{r,liq} = 0.04184\,[3.85 + (0.035\,T - 0.41)\,\alpha] \quad \text{(A.16)}$$

** Predicted temperatures within the simulation are converted to °C so that the empirical relationships can be used.*

*** Average value taken from* [52,53]

Table A.5. Properties and parameters used for glass fibre fabric.

Property/Parameter [units]	Value	Source
Transverse thermal conductivity of impregnated GF fabric, $\kappa_{c,T}$ [W/m K]*	Equation A.17	[55]
Thermal conductivity of glass fibre, κ_f [W/m K]	0.417	[67]
Thermal conductivity of dry GF fabric, κ_{fab} [W/m K]	0.2	[57]
Density of E-glass fibre, ρ_f [kg/m^3]	2560	[68]
Specific heat capacity of E-glass fibre, $c_{P,f}$ [J/kg K]	810	[26]
Inter-tow permeability of stitched GF fabric, K_1 [m^2]**	13.675×10^{-10}	[20]
Intra-tow permeability of GF K_2 [m^2]	Equation A.18	[58]
Glass fibre radius, R_{fib} [m]	8.0×10^{-6}	[69]
Fibre volume fraction of glass fibre tow, $V_{f,tow}$	0.67	[45]

$$\frac{\kappa_{c,T}}{\kappa_r} = \frac{1}{4}\left[\sqrt{\left(1-V_f\right)^2\left(\frac{\kappa_f}{\kappa_r}-1\right)^2+\frac{4\kappa_f}{\kappa_r}}-\left(1-V_f\right)\left(\frac{\kappa_f}{\kappa_r}-1\right)\right]^2 \quad \text{(A.17)}$$

$$K_2 = K_{\perp quad} = \frac{16}{9\pi\sqrt{2}}\left[\sqrt{\frac{\pi}{4V_{f,tow}}}-1\right]^{5/2} {R_{fib}}^2 \quad \text{(A.18)}$$

** The Springer-Tsai model* [70] *can also be used with little change to the overall result.*

*** Average value for stitched GF fabric.*

Table A.6. Properties used for bagging and tooling materials.

Property [units]	Value	Source
Thermal conductivity of bagging [W/m K]	0.069	[59]
Thermal conductivity of aluminium [W/m K]	216.3	[59]
Thermal conductivity of tool steel [W/m K]	53.35	[51]
Density of bagging [kg/m^3]	355.6	[59]
Density of aluminium [kg/m^3]	2692.1	[59]
Density of tool steel [kg/m^3]	7822.8	[51]
Specific heat capacity of bagging [J/kg K]	1256.0	[59]
Specific heat capacity of aluminium [J/kg K]	916.9	[59]
Specific heat capacity of tool steel [J/kg K]	485.0	[51]

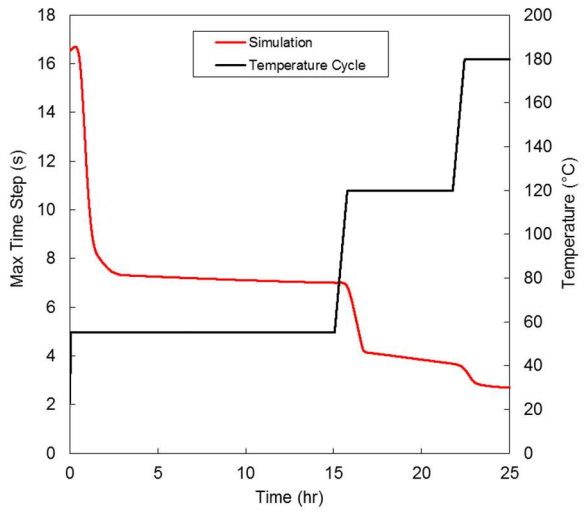

Figure A.1. The maximum allowable time step to achieve a stable solution for a GF/Epoxy-powder ply. The curing and compaction during the cycle causes the thermal diffusivity, γ, and the spatial increment, Δz, to change. This results in the max time step being reduced.

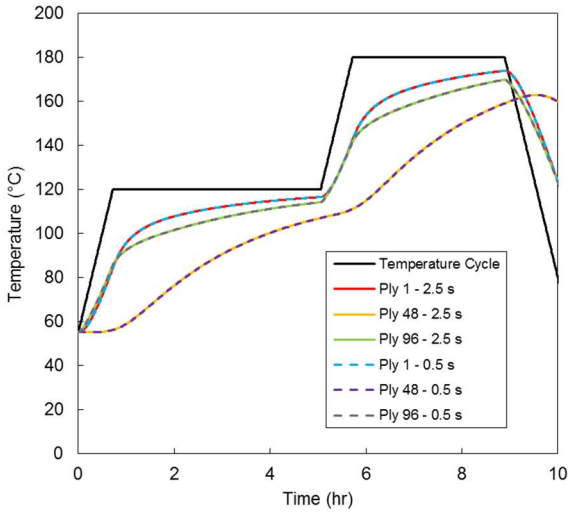

Figure A.2. Test of simulation accuracy for two time step sizes: 0.5 s, and 2.5 s. Heat transfer through a 96-ply GF/Epoxy-powder laminate is simulated with a 10 mm steel tool.

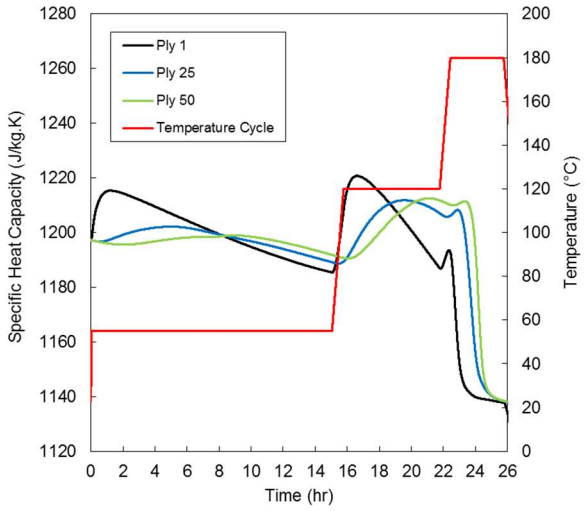

Figure A.3. Plot of the specific heat capacity variation during the temperature cycle. It increases with temperature, and it decreases with the advancement of cure.

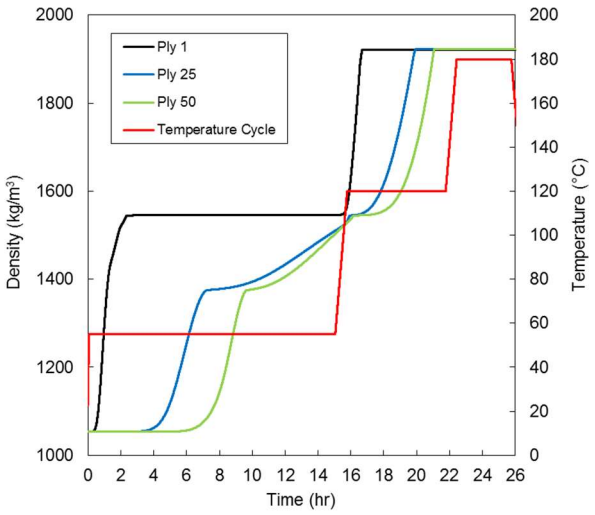

Figure A.4. Plot of the density variation of the plies during the temperature cycle. The ply density increases as the epoxy powder sinters and infuses into the fibre-bed.

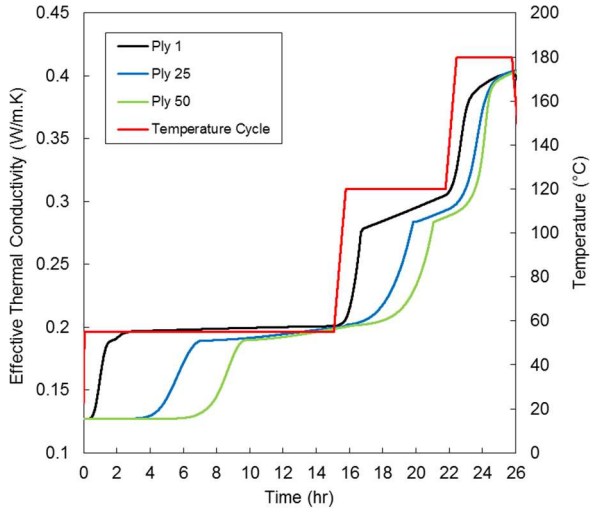

Figure A.5. Plot of the effective thermal conductivity variation during the temperature cycle. It increases with temperature, and is also affected by sintering of the powder and impregnation of the fibre-bed. The values are back-calculated from the thermal resistances of each ply.